Structure–Activity Optimization of Luminescent Tb-doped LaF3 Nanoparticles

Mohammed Rahali, Charlotte Heinritz, Agnès Hagège, Pascale Ronot, Anne Boos, Loïc Charbonnière, Clémence Cheignon

To cite this version:

Mohammed Rahali, Charlotte Heinritz, Agnès Hagège, Pascale Ronot, Anne Boos, et al.. Structure–Activity Optimization of Luminescent Tb-doped LaF3 Nanoparticles. Inorganic Chemistry, 2024, 63 (27), pp.12548-12555. 10.1021/acs.inorgchem.4c01475 . hal-04635080

HAL Id: hal-04635080
https://hal.science/hal-04635080v1

Submitted on 4 Jul 2024

Structure-activity optimization of luminescent Tb doped LaF_3 nanoparticles

Mohammed A. Rahali,[1] *Charlotte L. Heinritz,* [1] *Agnès Hagège,*[2] *Pascale Ronot,*[3] *Anne Boos,*[3] *Loïc J. Charbonnière,*[*1] *Clémence Cheignon*[*1]

[1] Equipe de Synthèse Pour l'Analyse (SynPA), Institut Pluridisciplinaire Hubert Curien (IPHC), UMR 7178 CNRS/Université de Strasbourg, ECPM, Bâtiment R1N0, 25 rue Becquerel, 67087 Strasbourg, Cedex 2, France

[2] Université Claude Bernard Lyon 1, ISA, UMR 5280 CNRS, 5 rue de la Doua, 69100 Villeurbanne, France

[3] Université de Strasbourg, CNRS, IPHC UMR 7178, F-67000 Strasbourg, France

KEYWORDS

Luminescence, nanoparticles, spectroscopy, morphology, Lanthanide

ABSTRACT

A series of Tb doped LaF_3 nanoparticles (NPs) was prepared by systematically varying the Tb doping rate from 0 to 100%. The elemental composition was confirmed by ICP-AES analysis and the size, morphology and crystal structure were determined in the solid state by transmission electron microscopy and X-ray diffractometry, while the size and zeta potential of the NPs in solution were studied by dynamic light scattering, Taylor dispersion analysis and laser Doppler electrophoresis. While the crystal structure appears to be hexagonal for doping rate up to 70%, an admixture of hexagonal and orthorhombic phases is observed for 80 and 90% Tb contents with a pure orthorhombic phase being obtained for TbF_3. The spectroscopic properties of the NPs were studied for bare NPs and in the presence of dipicolinic acid as surface capping antenna ligand in solution. The coverage of the NPs by the ligand resulted in an increase of the luminescence lifetime of the emitting Tb centers, as a consequence of a better protection towards luminescence quenching from water molecules, as well as a large improvement of the brightness of the NPs. Taking into account the various parameters, a doping rate of 40% Tb was shown to be the best compromise for the development of such NPs for bio-analytical applications.

Introduction

Photoluminescent nanoparticles (NPs) are very attractive probes for (bio)analytical applications and imaging[1] and have evolved during the last decades to become a key component of the (bio)analysis and biomedical research. They are characterized by large surface-to-volume ratios, favoring the loading of photoluminescent entities such as organic compounds, complexes or elements, making them very bright probes compared to single photoluminescent entities. Among them, lanthanide containing nanoparticles (Ln-NPs) are a very special class of nanomaterials exhibiting the unique optical properties of Ln such as specific and sharp emission bands, long luminescence decay time allowing time-resolved measurements with very low auto-fluorescence background noise, large Stokes' shift and good photostability.[2] However, due to the forbidden nature of the 4f-4f transitions from which the optical properties of Ln^{3+} ions arise, their very weak absorptivity makes direct excitation inefficient. This can be overcome either by using a powerful excitation source (laser) as commonly applied for upconversion Ln-NPs,[3,4] or by the antenna effect,[5] an indirect Ln photosensitization pathway using light-harvesting chromophoric ligands. Photosensitized Ln-NPs reported in the literature can be divided into three categories:[6] (i) Ln doped inorganic NPs with surface capping antennas; (ii) polymeric NPs encapsulating Ln complexes; (iii) (in)organic NPs surface functionalized by Ln-complexes. The advantages of the first category are their very long lifetimes, especially for Tb^{3+} ions,[7] originating from the protection of the atom in the NP from deactivation caused by the environment, and exceptional brightness, that can exceed those of Quantum Dots and semi-conducting nanopolymers, as previously demonstrated.[8] Indeed, a microwave-assisted synthetic protocol in water was proposed to obtain Tb doped LaF_3 NPs of diameter *circa* 20–25 nm (determined by TEM) with a 10% doping rate.[8] When capped by appropriate light-harvesting coordinating ligands, they are highly luminescent and exhibit an exceptional brightness up to 2.2×10^6 mol.L^{-1}.cm^{-1} along with a very long excited state lifetime (3.76 ms). Such NPs have been shown to be efficient luminescent probes for Förster Resonance Energy Transfer (FRET) based (bio)sensing,[9] immunoassays[10] and *in vivo* imaging.[11] Various antennas have been tested to improve the luminescence properties of the NPs, however the Tb doping rate is also an important factor to be considered. We here report the design of $Tb_xLa_{1-x}F_3$ NPs with various doping rates of Tb (x = 0 to 1 with 0.1 steps) and the comparison of their size, colloidal stability, crystal structure and luminescence properties in order to find the most promising luminescent probe for (bio)analytical applications.

Results and Discussion

Preparation of the Tb doped NPs

Eleven types of $Tb_xLa_{1-x}F_3$ were prepared in aqueous solution under microwave irradiation by adaptation of reported protocols.[8,12] The total Ln concentration remained unchanged and the desired Tb doping rate (x = 0, 0.1, 0.2, 0.3, 0.4, 0.5, 0.6, 0.7, 0.8, 0.9, 1) was obtained by adapting the La/Tb stoichiometry in the NPs. The resulting Tb doping rates (Table 1), obtained from ICP-AES measurements, are in line with the theoretical rates, highlighting the good control of the doping rate by the NP preparation procedure. The detection of a tiny percentage of Tb in the supposedly pure LaF_3 NPs is assumed to originate from the purity of the $LaCl_3$ starting material and contamination *via* the synthesis glassware used for all the Tb doped NP preparation.

Table 1: Theoretical Tb doping rates (%) of the various $Tb_xLa_{1-x}F_3$ NPs and the corresponding experimental doping rates, calculated from Tb and La concentrations measured by ICP-AES (Table S1).

Theoretical Tb rate (%)	Experimental Tb rate (%)
0	0.52 ± 0.04
10	10.9 ± 0.1
20	20.3 ± 0.1
30	29.3 ± 0.2
40	38.6 ± 0.4
50	48.3 ± 0.6
60	58 ± 1
70	69.6 ± 0.6
80	79.8 ± 0.8
90	89.5 ± 0.7
100	99.9 ± 0.7

Characterization of Tb doped NPs

X-Ray diffractograms of the series of Tb doped NPs are presented in Figure 1. XRD patterns of LaF_3 NPs with Tb doping from 0 to 70% are consistent with the hexagonal LaF_3 phase (COD 1010983).

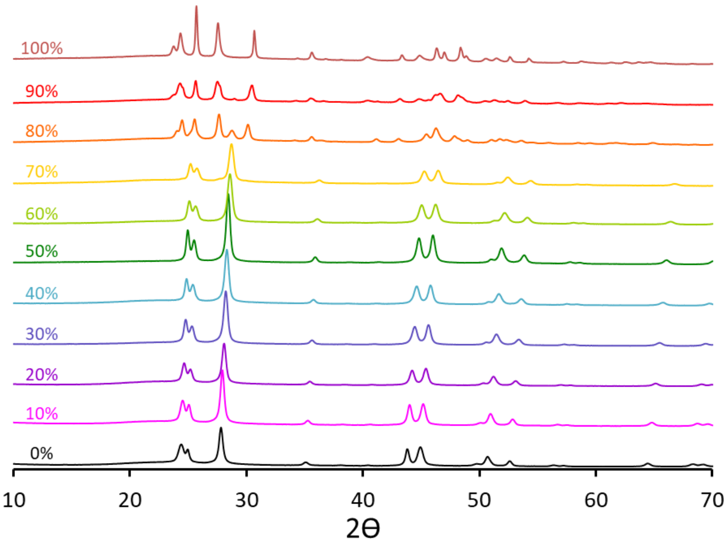

Figure 1: X-ray diffraction pattern of Tb doped LaF_3 NPs. The percentages indicated correspond to the Tb doping rates in the NPs.

The dependence of the unit cell dimensions (see hexagonal lattice parameters calculated in Table S2) to the doping level of Tb (Figure 2) confirms that this system follows Vegard's law[13] as the unit cell parameters linearly depend on the dopant concentration. Thus, Tb^{3+} ions isomorphically substitute La^{3+} ions in the hexagonal LaF_3 structure. The decrease of unit cell parameters with increasing Tb content originates from the Ln contraction, as the ionic radius of Tb^{3+} is 11% smaller than the ionic radius of La^{3+}.[14]

While the peaks of the TbF_3 NPs diffractogram were assigned to a standard TbF_3 orthorhombic phase (COD 1530594), 80 and 90% Tb NPs XRD revealed the coexistence of both hexagonal LaF_3 and orthorhombic TbF_3 lattices. This concomitance of two different lattices inside individual nanocrystals has already been observed in GdLaF$_3$ NPs, reported by Brixton *et al.* and occur for LaF$_3$ NPs doped with 50 to 75% Gd.[15] Similarly, Liang *et al.* detected it in GdF$_3$ doped with less than 30% La.[16] Various phases (hexagonal/cubic,[17] hexagonal NaYF$_4$/hexagonal LaF$_3$[18]) were also observed in Ln doped NaYF$_4$ NPs or in Lu$_{1-x}$In$_x$FeO$_3$ films (orthorhombic/hexagonal mixed-phase) with specific doping levels.[19]

Our results are in line with the study made by Liang *et al.* for La doped GdF$_3$[16] as the two-phases coexistence is observed for the same La content (lower than 30%) even though the dopant was different (Gd *vs* Tb) but with very similar ionic radii.[14]

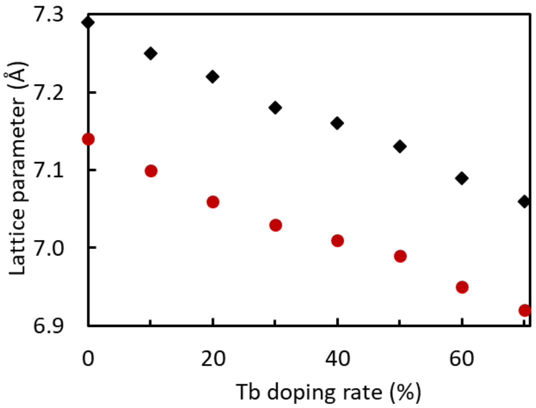

Figure 2: Hexagonal lattice parameters of the unit cells from 0 to 70% Tb doped LaF$_3$ NPs. Red dots correspond to a = b and black dots to c.

The colloidal stability of the NPs was then investigated by estimating their surface charge through zeta potential determination (Figure 3). As it is considered that a zeta potential value higher than |30| mV indicates a good nanosuspension behaviour,[20] it can be concluded that LaF$_3$ NPs with a Tb doping rate up to 60% have a good dispersion in solution. Moreover, their surface charge increases with the Tb content, before dropping drastically to zeta potential values close to 30 mV for Tb percentage higher than 60%, correlated with the TbF$_3$ orthorhombic lattice appearance in the NPs (except for 70%Tb NPs). These latter values could indicate a colloidal instability leading to NP aggregation.

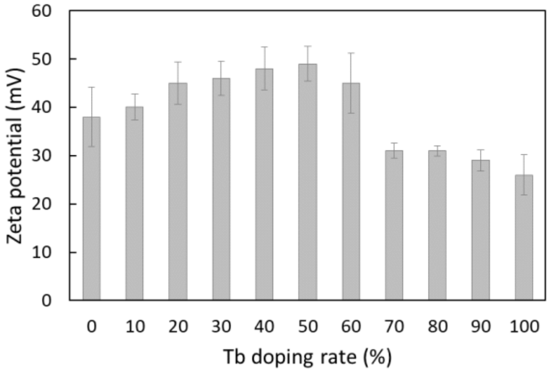

Figure 3: Zeta potential (mV) of Tb doped LaF_3 NPs determined by laser Doppler electrophoresis (LDE) measurements (Figures S1 and S2) for the different Tb doping rates. Measurements were realized at pH 4.8 ± 0.2 (pH of each batch is indicated in Figure S3) to obtain comparable results.

Hydrodynamic diameters (D_H) were determined by Dynamic Light Scattering (DLS) and Taylor Dispersion Analysis Coupled to Inductively Coupled Plasma-Mass Spectrometry [21] (TDA-ICP-MS, Figure 4). It is worth noting that DLS measurements were performed directly on the NP stock solution or two times diluted solution in water whereas the NP samples for TDA-ICP-MS measurement were prepared by a 30 times dilution in a TBS solution at pH 7.4 with the addition of sodium citrate. As shown in Figure 4, while the D_H determined by DLS is generally lower than by TDA-ICP-MS, same trends are observed with both techniques. The introduction of Tb in the LaF_3 matrix leads to a constant increase of the NP size, with the exception of 80% Tb doped NPs that are smaller than the 70%. Moreover, the highest values reaching a hundred nm are obtained for 90% Tb and TbF_3 NPs. For those two NPs, D_H determination was very complex by DLS, as illustrated by the high error bar for 90% Tb and the impossibility to obtain reliable values for TbF_3 NPs. Two hypotheses could explain this issue: (i) NPs may aggregate, as supported by the low zeta potential measured, leading to a heterogeneous sample or (ii) NPs are not spherical as it is assumed for the D_H determination by both techniques.

The abrupt increase of the size of the NPs for high Tb doping rate is strongly related to the change of the crystallographic phase from hexagonal, for low doping, to orthorhombic at doping rate exceeding 90%.

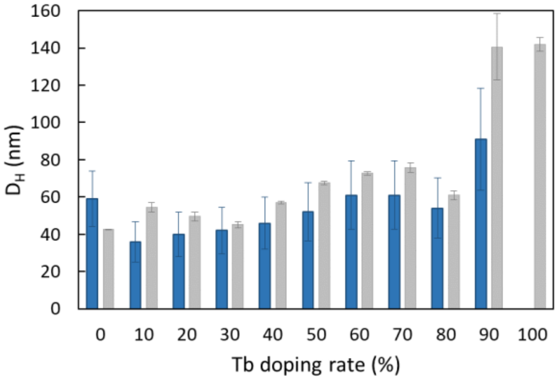

Figure 4: Hydrodynamic diameters (D_H) of Tb doped LaF_3 NPs determined by DLS (blue bars) and TDA-ICP-MS (grey bars) respectively for the different Tb doping rates. Size distributions measured by DLS and taylorgrams for each NP batch are shown in Figures S4-5 and S6 respectively.

Transmission Electron Microscopy (TEM) images (Figure 5) confirmed the previous assumptions. Indeed, although LaF_3 NPs are not perfectly spherical (Figure 5a), 90% Tb NPs (Figure 5e) are very elongated and especially more aggregated, while TbF_3 NPs (Figure 5f) have a needle-like morphology with formation of star-like aggregates. NPs with Tb doping level from 0 to 70% present a similar morphology (Figure 5a-c for 0, 60 and 70% and Figure S7 for other samples), with the presence of lighter rounded zones inside the NP. This particular structure is described in the literature as a hollow-like morphology, reported to be related to the hexagonal structure of the LaF_3 NPs as it is not or rarely observed in orthorhombic structures.[22–24]

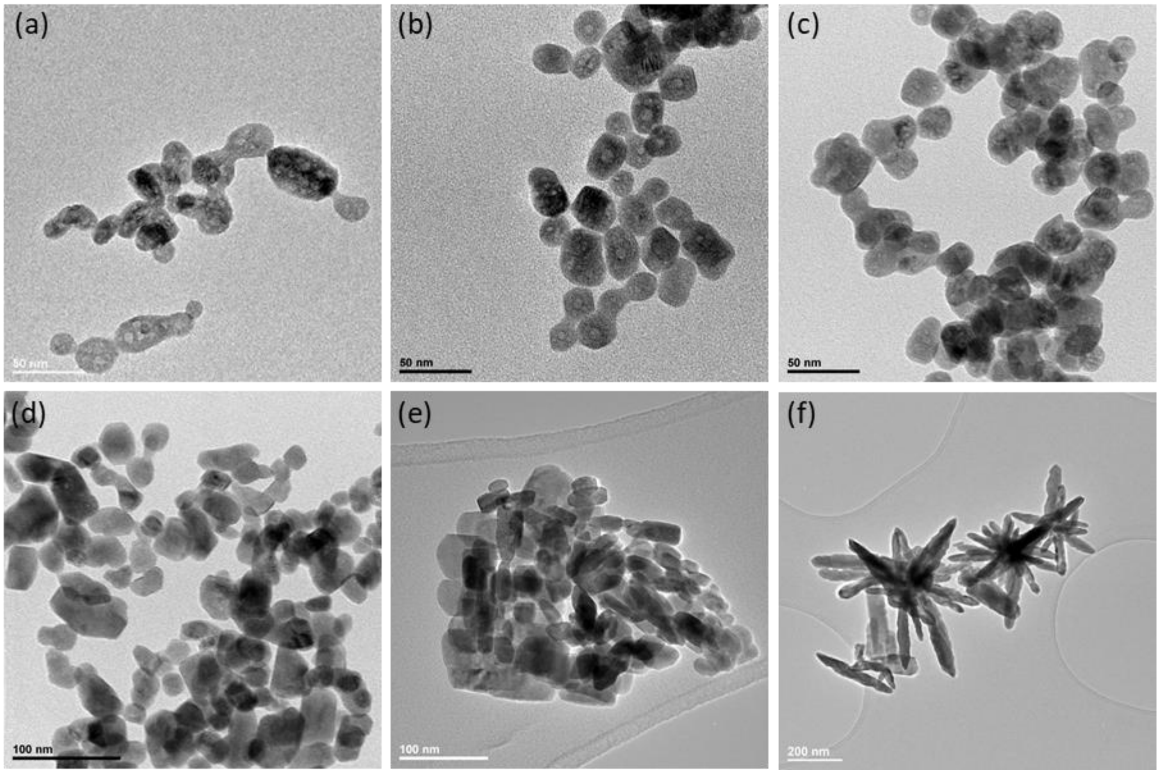

Figure 5: TEM images of (a) 0%, (b) 60%, (c) 70%, (d) 80%, (e) 90% Tb doped LaF_3 NPs and (f) TbF_3 NPs.

This is in line with the XRD data as an orthorhombic lattice is present in the NPs up to 70% Tb doping level, and TEM images confirm the absence of hollow-like structure for doping rates higher than 70% (Figure 5d-f). From TEM images, length and width of 200 to 300 individuals of each batch were measured (see Figures S8 and S9) and a mean NP diameter was determined (Figure 6), except for the needle-like TbF_3 NPs for which such an averaging is irrelevant. NP diameters are increasing from 20 to more than 30 nm with increasing Tb content up to 50%, as it was previously noticed with D_H.

With the exception of 90% doped Tb NPs and TbF_3 NPs that have the tendency to aggregate and whose sizes are not well controlled during the synthesis, the Tb doped LaF_3 NPs are suitable for (bio)analytical applications.[2,6,25]

From the diffractograms, the crystal sizes of the different NP batches were also determined using the Scherrer equation (Figure 6, blue bars), highlighting NPs with crystallite sizes of 15 to 20 nm except for TbF_3 NPs that appear to be much bigger with a high dispersity (30 ± 15 nm). The sizes of the crystalline domains obtained by the Scherrer equation are globally in good agreement with those obtained from TEM data (Figure 6, grey bars), pointing to the uniformity of the crystallinity of the NPs. The slightly larger sizes obtained by TEM may be induced by the biases inherent to the spherical model used to determine sizes in TEM images. An important difference is nevertheless observed for 90% doped NPs whose particle size is more than twice higher than the crystallite size, suggesting that the NPs could be made up of several crystallites.

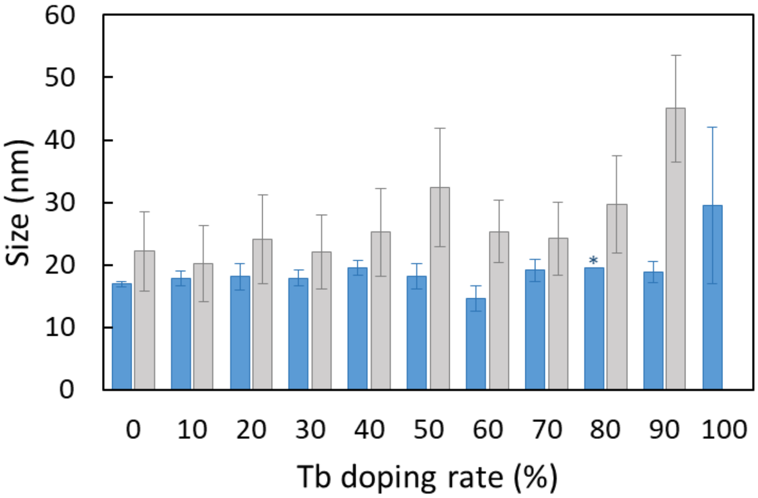

Figure 6: Particle size determined by TEM (grey bars) and crystallite size calculated from Scherrer equation (blue panel) of Tb doped LaF_3 NPs for the different Tb doping rates.*For 80% Tb doped NPs, only one peak was accessible for the measurement of its area.

An estimation of the molar concentration of NPs was determined following a published method,[8] by using the mean NP diameter calculated from TEM images, the density of $La_{1-x}Tb_xF_3$ calculated as the percentage weighted density of TbF_3 and LaF_3 and the concentration of La and Tb in solution obtained by ICP-AES analysis. Concentration of NP stock solutions in water was typically found in the 10^{-7} $mol.L^{-1}$ range (see Table S1 for detailed concentrations).

Photoluminescence properties of Tb doped NPs

As mentioned previously, the direct excitation of Tb is very inefficient because of its very low absorptivity.[26] Thus, dipicolinic acid (DPA) was chosen as antenna to indirectly excite Tb ions in the NPs, as it has been reported to be a very good Tb photosensitizer in complexes[27,28] and as capping antenna for the NPs.[8,29] Time-resolved excitation spectra of bare and DPA capped 20% Tb doped NPs (Figure S10; emission of Tb at 545 nm) show the appearance of an intense and broad excitation band at 270 nm in the presence of DPA, illustrating the antenna effect.

Spectroscopic titrations of the various Tb doped NPs by DPA ligand were realized. Increasing quantities of ligand were added to an HEPES solution (10 $mmol.L^{-1}$, pH 7.0) containing a fixed NP amount and the time-gated emission spectra of the solutions upon excitation into the maximum of the excitation band of DPA (270 nm) were monitored, as illustrated in Figure 7 for $La_{0.9}Tb_{0.1}F_3$ NPs. The introduction of DPA ligands in the solution resulted in the observation of four main emission bands at 485, 545, 590 and 620 nm, corresponding to the typical $^5D_4 \rightarrow {}^7F_J$ (J = 6 to 3 resp.) electronic transitions of Tb. The $^5D_3 \rightarrow {}^7F_J$ emission bands (in the 350-450 nm range) are never observed whatever the Tb doping level (as shown in Figure S11 for 20% Tb doped NPs as an example). These emission bands are reported in the literature for low Tb concentration in Tb doped materials and for higher Tb contents, their intensity decreases due to Tb-Tb cross-relaxation energy transfer (CRET) along with the increase of green emission bands.[30,31] Unfortunately, the contribution of CRET as a function of Tb doping rate cannot be investigated here, as the emission from $^5D_3$ level is not visible in our conditions.

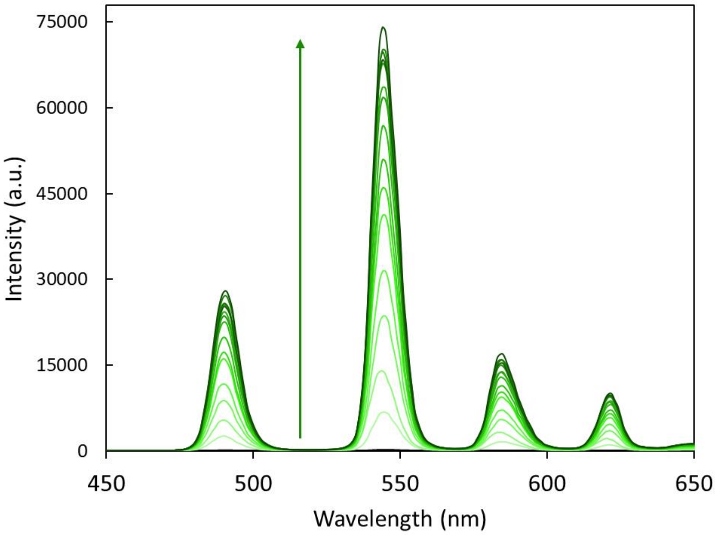

Figure 7. Evolution of the TR emission spectra of a 5.5 10^{-10} mol.L^{-1} solution of $La_{0.9}Tb_{0.1}F_3$ (HEPES 50 mmol.L^{-1}, pH 7.0) upon addition of DPA (0 to 10 μmol.L^{-1}; from light green to dark green). λ_{exc} = 270 nm; delay time of 50 μs; integration time of 2 ms.

The evolution of the $^5D_4 \rightarrow {}^7F_5$ transition band (at 545 nm) as a function of the increasing DPA amount is represented, the results being normalized either by the total Ln concentration (Figure 8a) or by the NP molar concentration (Figure S12a) in order to compare the titrations of the various NP batches. For every batch of NPs, the emission intensity increases with the increased DPA amount before reaching a plateau (Figure 8a), showing that the NP surface is fully covered by the ligands. By comparing the intensities at the plateau for each Tb doping rate (Figure 8b), it can be observed that the maximal intensity increases with the Tb doping rate and reaches a maximum for

40 to 60% Tb contents. A dramatic decrease is then observed for NPs with 80% and higher Tb rates, that can be correlated with the partial crystal lattice change from hexagonal to orthorhombic phase.

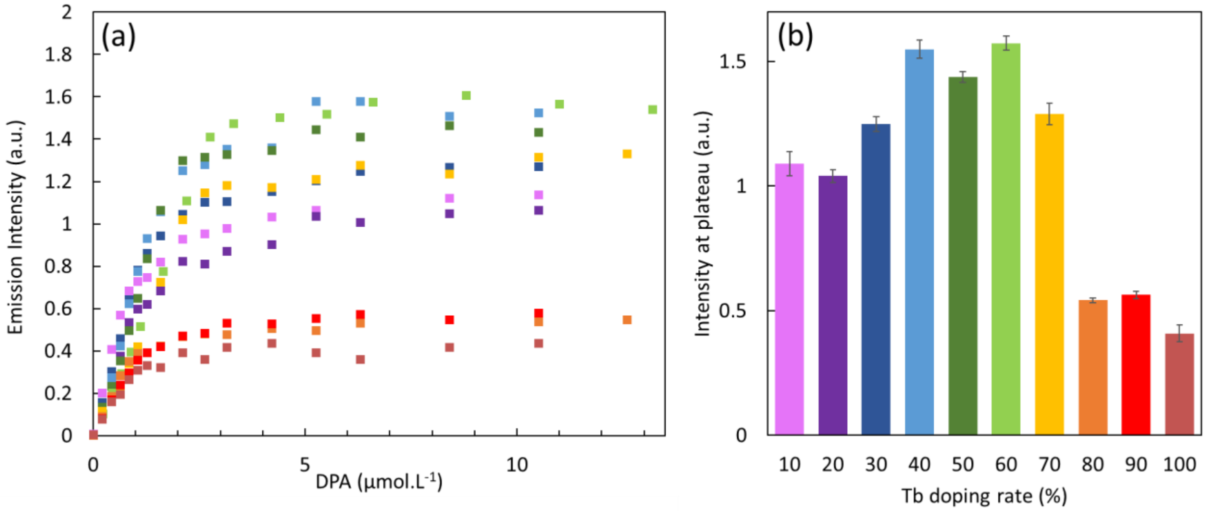

Figure 8: (a) Evolution of the Tb centered emission intensity at 545nm ($^5D_4 \rightarrow {}^7F_5$ transition) as a function of the DPA concentration (µmol.L^{-1}) and (b) intensity measured at the plateau for NPs containing 10 (pink), 20 (purple), 30 (dark blue), 40 (light blue), 50 (dark green), 60 (light green), 70 (yellow), 80 (orange), 90 (light red) or 100 (dark red) % of Tb. Titrations made in HEPES buffer (10 mmol.L^{-1}, pH 7.0) with NP solutions corresponding to a total Ln concentration of exactly *circa* 7 × 10^{-5} mol.L^{-1} and normalized by the total Ln concentration for comparison (λ_{exc} = 270 nm).

The same trend is observed for the emission intensity normalized by the NP molar concentration (Figure S12a and S12b), with the exception of 50% and 90%Tb doped NPs that have a much more intense emission than 40% and 60%Tb NPs and than 80%Tb NPs respectively. This originates from their average mean diameter determined by TEM that is higher than the other batches. However, it can be observed that these NPs have a very large size distribution (see Figure S9), thus the data normalized by the NP molar concentration (calculated using the average TEM related diameter) should be considered with caution. Nevertheless, a number of DPA per NP at the equivalence has been calculated from these data (Figure S12c), determined by the intersection of the initial and final tangents of the curve. This gives an approximate information of the number of DPA required to saturate the NP surface (from 2500 to 12500 DPA/NP depending on the NP size).

The luminescence properties of the NPs were also investigated through the record of temporal photoluminescence intensity decays of both bare NPs (Figure S13) and DPA covered NPs (Figure S14; number of DPA per NP determined previously as the equivalence in Figure S12c). For all the Tb doped NPs, excited at 270 nm, a bi-exponential Tb-centered emission is observed, with the determination of a lifetime composed of two main components as previously reported[11] (the two components are reported in Table S3). The longer one is attributed to the Tb ions that are protected in the core of the NP and the shorter one corresponds to Tb ions at the NP surface, that suffer from photoluminescence quenching by the aqueous solvent. A clear trend observed is that the short component lifetime systematically increased when the NPs are capped with DPA ligands. The protection offered by the tridentate ligands to surface Ln atoms decreased the non-radiative deactivation pathways for these ions, resulting in an increase of their lifetime. However, it is far more difficult to draw clear conclusions from the lifetime values or their relative proportions for two main results. For bare NPs, excitation at 270 nm is performed directly in the high energy *f-f* transitions of Tb. Assuming in first approximation similar absorption cross sections for inner and surface Tb atoms, this results in a larger excitation of the core Tb atoms, more abundant than the surface ones. In contrast, excitation at the same energy in the presence of DPA ligands will result in a preferred excitation of the surface Tb atoms via the antenna effect, rendering the comparison of bare/capped lifetimes or proportions difficult. As a second point, cross relaxation between Tb atoms are expected to occur with energy hoping between surface and core Tb atoms. These processes will be strongly dependent on the Tb doping ratio, on the one hand, and in preferred directions, depending on the presence or not of DPA (from the core to the surface for bare NPs, the reverse for DPA capped NPs). For these two reasons, a direct comparison of both lifetimes and proportionality factors appeared to be hazardous in our hands. From these data, a weighted average lifetime $< \tau >$ was calculated[32] by taking into account the fractional contribution f of both core and surface Tb in the emission and their respective lifetimes τ:

$$< \tau >= \sum_{i=1}^{n} f_i \tau_i$$

$$\text{with } f_i = \frac{\alpha_i \tau_i}{\sum_{i=1}^{n} \alpha_i \tau_i} \text{ and } \sum_{i=1}^{n} f_i = 1$$

where α is the pre-exponential factor of amplitude.

The weighted average photoluminescence lifetimes are shown in Figure 9. Lifetimes between *ca*. 1.5 ms and 2.3 ms are measured for low Tb doping levels in bare NPs (grey bars) and drop to values between 0.7 and 1.1 ms with doping rates higher than 50%Tb. The values are generally higher following the addition of the antenna (Figure 9, green *vs* grey bars), the latter protecting the NP from solvent quenching, except for 10 and 40% doping ratii, showing a reverse trend, but with differences that are within experimental errors. After surface coverage by DPA, a clearer tendency is observed as the lifetime increases up to 2.7 ms for 20%Tb, before linearly decreasing by up to 1.5 ms for 50%Tb doping rate and then remaining quite constant. A decrease of lifetime values is noted from 50-60%Tb for both bare and DPA capped NPs, that most probably originates from concentration quenching.[33] This phenomenon is generally observed beyond 5mol% dopant for bare Ln doped nanocrystals,[34] however Prasad and colleagues demonstrated with upconverting Nd doped $NaYF_4$ NPs that the optimal doping concentration can be shifted from 2 to 20mol% thanks to surface capping organic dye photosensitization.[35]

It is worth noting that an unclear behavior is obtained for bare 90% Tb NPs that exhibit a higher average lifetime (1.1 ms) compared with their orthorhombic counterparts (80% Tb NPs and TbF_3 NPs) while no significant difference is seen when covered by DPA.

Among all NPs, a Tb doping of 20% leads to longest lifetimes for both bare and DPA covered NPs (2.3 and 2.7 ms respectively).

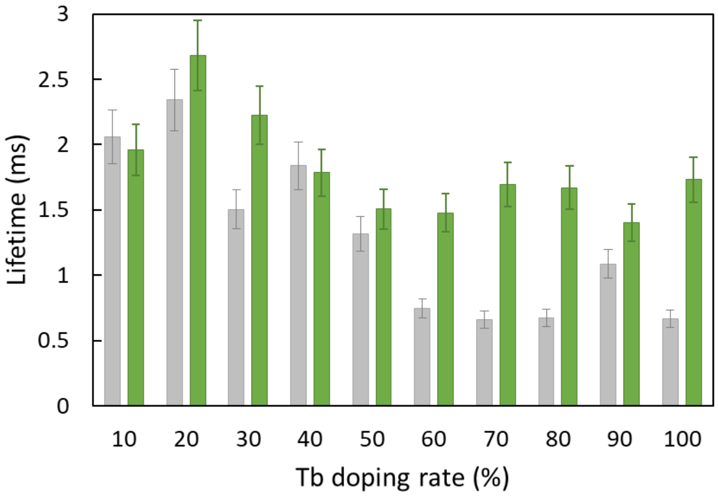

Figure 9: Weighted average photoluminescence lifetimes of bare Tb doped LaF_3 NPs (grey bars) or Tb doped LaF_3 NPs covered with DPA (green bars), calculated from photoluminescence intensity decays (Figures S13 and S14).

Conclusion

From a rapid and simple microwave-assisted synthesis in water, a series of Tb doped LaF_3 NPs with various doping rates was prepared. Thanks to a large panel of techniques (TEM, DLS, TDA-ICP-MS, zeta potential, XRD), the size, morphology, colloidal stability and crystal structure of the NPs were meticulously investigated. The spectroscopic properties (time-resolved emission and lifetimes) of both bare NPs and NPs photosensitized by various quantities of the capping antenna (dipicolinic acid, DPA) were examined.

The crystal lattice composing the NPs has been shown to have an important impact on both their physical and optical properties. NPs with Tb doping levels up to 70% display a hexagonal LaF_3 lattice while an orthorhombic TbF_3 phase appears for higher Tb contents, in coexistence with the hexagonal LaF_3 phase for 80 and 90% Tb, and in a pure orthorhombic TbF_3 phase for TbF_3 NPs. The lattice change from hexagonal to orthorhombic leads to drastic modifications in the morphology of the NPs and the spectroscopic properties are widely affected. Thus, it appears that a host matrix with only hexagonal LaF_3 lattice is mandatory to obtain small rounded NPs with long Tb excited-state lifetimes and a higher photoluminescence emission.

From this series, the 40% Tb doped LaF_3 NPs arise as the best probe candidate, being among the most colloidally stable, monodisperse rounded NPs and exhibiting an average luminescence lifetime of 1.8 ms and the highest emission through DPA photosensitization. With improved luminescence properties compared to the already studied 10%Tb doped NPs, such a luminescent probe would be very appealing to push forward the development of (bio)analytical assays that require a higher sensitivity as obtained thanks to the background free time-resolved detection mode,[36] for ELISA type assays[37,38] or for the detection of specific analytes depending on their coordination ability towards Ln atoms.[39]

Experimental section

Synthesis of the nanoparticles

A solution of NH_4F (0.72 mol.L^{-1}, 3.51 mL) in water was added dropwise to a stirred aqueous mixture of $TbCl_3$ (0.05 mol.L^{-1}, x mL) and $LaCl_3$ (0.05 mol.L^{-1}, $16 - x$ mL) at room temperature with a volume « x » between 0 and 16 mL depending on the desired Tb doping rate. It results in the formation of a turbid solution. The mixture was heated in a microwave oven at 150°C for 12 min. After cooling, the precipitate was collected by centrifugation at 9000 rpm for 25 min. The isolated solid was dispersed in milliQ water (20 mL) with sonication at 60°C for 30 min. The Tb and La content of the obtained solutions was determined by ICP–AES.

NP characterization methods

ICP–AES analysis of samples in water were performed on a Varian 720 spectrometer equipped with a quartz Meinhard nebulizer and a cyclone spray chamber. In a typical experiment, the mother solution of NPs was sonicated for 30 min in an ultrasound bath, and was strongly agitated on a vortex before a sample (1 mL) was collected by pipetting. The sample was mineralized with high-purity nitric acid (3 mL) by heated in a microwave oven at 200°C for 50 min. The concentration was then determined by ICP–AES spectrometry by comparison with certificate standard samples.

The XRD pattern was recorded at room temperature using a Brucker D8 Advance diffractometer equipped with a monochromatic copper radiation source ($K_\alpha = 1.54056$) and a Vantec detector working at 40 kV and 40 mA in the 20–90° 2θ region with a scan step of 0.028°. Diagrams were processed using the COD (crystallographic open database) and the Diffrac Eva processing tool. The crystal sizes were determined as the mean value for three reflexes using the Scherrer equation. For this purpose, the areas of the reflexes with hkl 112, 223 and 211 were measured for samples with hexagonal structure and the reflexes with hkl 121, 002 and 321 for samples with orthorhombic structure. Transmission electron microscopy (TEM) was performed using a JEOL 2100 LaB6 microscope with a point resolution of 0.22 nm, and operating at 200 kV acceleration voltage. A drop of the suspension of NPs in water was deposited on TEM grids. The grid was prepared with a porous membrane covered by an amorphous carbon layer. From TEM images, length and width of 200 to 300 individuals of each batch were measured and a mean NP size was determined.

The zeta potential and the hydrodynamic diameter were measured using an AMERIGO system (Cordouan technologies). All measurements were done in milliQ water at room temperature. DLS measurements were performed using an external probe with laser wavelength at 638 nm. The experimental correlograms are fitted by SBL mathematical algorithm and the particle size histograms were reported in number representation. Laser Doppler electrophoresis measurements were performed 5 to 20 times diluted solutions from stock solution at 20.27 V/cm applied electric field. Zeta potential is directly correlated to the mobility of NPs according to the theory of Smoluchovski. Results are given as the mean value of at least 6 measurements with their standard deviations.

TDA experiments were conducted using a TDA-ICP-MS hyphenation between a 7100 capillary electrophoresis instrument (Agilent) and a Nexion 300X ICP-MS (Perkin Elmer), described elsewhere.[21] Fused silica capillaries with an inner diameter of 75 μm and outer diameter of 375 μm, and a total length of 70 cm, were coated with hydroxypropylcellulose (HPC) using a solution of 0.05 $g.mL^{-1}$ in water. Twenty-μL sodium citrate 20 $mg.mL^{-1}$ were added to 10 μL nanoparticles suspensions and the mixture was sonicated for 1 h at 60°C. Before experiments, samples were diluted 10 times in TRIS 10 $mmol.L^{-1}$, NaCl 125 $mmol.L^{-1}$, pH 7.4. Samples were hydrodynamically injected (20 mbar for 3 s) and mobilized at a constant pressure of 35 mbar using TRIS 10 $mmol.L^{-1}$, NaCl 125 $mmol.L^{-1}$, pH 7.4. Detection was carried out by ICP-MS at m/z = 139 (for La) and 159 (for Tb) with a data acquisition rate of 500 ms $point^{-1}$. Between runs, the capillary was flushed at 1 bar for 5 min with the mobilization medium. Peak deconvolution was carried out using Origin 8.5 software.

Photoluminescence spectroscopy

Time-gated emission spectra were recorded at 25°C on a TECAN Spark multimode microplate reader with monochromators, working with a Xe flash lamp in low-binding black 96-wells microplates from Greiner bio-one.

For each batch of NPs, various quantities of DPA ligand in HEPES (pH 7.0, 10 mmol.L^{-1}) were added to HEPES buffered solution (pH 7.0, 10 mmol.L^{-1}) of $La_{1-x}Tb_xF_3$ NPs (concentration in the well is 500 times diluted compared to the NP stock solution, corresponding to a Ln concentration of *circa* 60 µmol.L^{-1}) in wells of a 96-well microplate. The plate was then agitated at 25°C for 10 min. and the time-gated emission intensity was recorded at 544 nm with a 5 nm bandwidth after an excitation at 270 nm (20 nm bandwidth) for each well. Time-resolved emission intensity was recorded under the following conditions: excitation at 270 nm with a bandwidth of 20 nm, emission measured at 544 nm with a bandwidth of 25 nm, a delay time of 50 µs and an integration time of 2 ms. To compare the results, the emission intensity was then normalized by the total Ln concentration or by the molar NP concentration calculated with the diameter determined from TEM images (see Table S1) for each NP batch.

Photoluminescence lifetimes were measured on an Edinburgh Instruments FLP920 spectrometer operating in the multichannel spectroscopy mode, using a Xe flash lamp as the excitation source. Errors in luminescence lifetimes were estimated to ±10%. Emission lifetimes of both bare and DPA covered NPs were recorded at room temperature, with a DPA concentration corresponding to a full coverage of the NP surface. The stock solutions of NPs were diluted 500 times in HEPES (10 mmol.L^{-1}, pH 7.0).

ASSOCIATED CONTENT

Supporting Information.

Elemental analysis of NPs and NP molar concentration determination; X-Ray diffraction studies; Determination of pH and colloidal stability of NPs; Hydrodynamic diameters determined by DLS and TDA-ICP-MS; TEM studies; Photoluminescence studies of NPs. (.pdf)

AUTHOR INFORMATION

Corresponding Authors

Loïc J. Charbonnière l.charbonn@unistra.fr

Clémence Cheignon ccheignon@unistra.fr

Author Contributions

The manuscript was written through contributions of all authors. All authors have given approval to the final version of the manuscript.

Funding Sources

This work was funded by the French National Research Agency (ANR) through the project ANR-21-CE19-0016-01 and is published with the support of the University of Strasbourg's IdEx program.

ACKNOWLEDGMENT

The authors acknowledge Lai Truong Phuoc who kindly realized the XRD measurements of the NPs. The TEM-Platform of IPCMS is acknowledged for TEM analyses.

ABBREVIATIONS

Dh, Hydrodynamic diameter; DLS, Dynamic Light Scattering; DPA, Dipicolinic acid; ICP-AES, Inductively coupled plasma atomic emission spectroscopy; LDE, Laser Doppler Electrophoresis; Ln-NPs, Lanthanide nanoparticles; NPs, nanoparticles; TBS, Tris Buffer Saline; TDA, Taylor dispersion analysis; TR, Time-resolved; XRD, X-Ray Diffractometry.

REFERENCES

(1) Algar, W. R.; Massey, M.; Rees, K.; Higgins, R.; Krause, K. D.; Darwish, G. H.; Peveler, W. J.; Xiao, Z.; Tsai, H.-Y.; Gupta, R.; Lix, K.; Tran, M. V.; Kim, H. Photoluminescent Nanoparticles for Chemical and Biological Analysis and Imaging. *Chem. Rev.* **2021**, *121* (15), 9243–9358. https://doi.org/10.1021/acs.chemrev.0c01176.

(2) Bao, G.; Wen, S.; Lin, G.; Yuan, J.; Lin, J.; Wong, K.-L.; Bünzli, J.-C. G.; Jin, D. Learning from Lanthanide Complexes: The Development of Dye-Lanthanide Nanoparticles and Their Biomedical Applications. *Coord. Chem. Rev.* **2021**, *429*, 213642. https://doi.org/10.1016/j.ccr.2020.213642.

(3) Malhotra, K.; Hrovat, D.; Kumar, B.; Qu, G.; Houten, J. V.; Ahmed, R.; Piunno, P. A. E.; Gunning, P. T.; Krull, U. J. Lanthanide-Doped Upconversion Nanoparticles: Exploring A Treasure Trove of NIR-Mediated Emerging Applications. *ACS Appl. Mater. Interfaces* **2023**, *15* (2), 2499–2528. https://doi.org/10.1021/acsami.2c12370.

(4) Wang, Y.; Zheng, K.; Song, S.; Fan, D.; Zhang, H.; Liu, X. Remote Manipulation of Upconversion Luminescence. *Chem. Soc. Rev.* **2018**, *47* (17), 6473–6485. https://doi.org/10.1039/C8CS00124C.

(5) Weissman, S. I. Intramolecular Energy Transfer The Fluorescence of Complexes of Europium. *J. Chem. Phys.* **1942**, *10* (4), 214–217. https://doi.org/10.1063/1.1723709.

(6) Cheignon, C.; Kassir, A. A.; Soro, L. K.; Charbonnière, L. J. Dye-Sensitized Lanthanide Containing Nanoparticles for Luminescence Based Applications. *Nanoscale* **2022**, *14* (38), 13915–13949. https://doi.org/10.1039/D1NR06464A.

(7) Li, S.; Zhang, X.; Hou, Z.; Cheng, Z.; Ma, P.; Lin, J. Enhanced Emission of Ultra-Small-Sized LaF_3:RE^{3+} (RE = Eu, Tb) Nanoparticles through 1,2,4,5-Benzenetetracarboxylic Acid Sensitization. *Nanoscale* **2012**, *4* (18), 5619–5626. https://doi.org/10.1039/C2NR31206A.

(8) Goetz, J.; Nonat, A.; Diallo, A.; Sy, M.; Sera, I.; Lecointre, A.; Lefevre, C.; Chan, C. F.; Wong, K.-L.; Charbonnière, L. J. Ultrabright Lanthanide Nanoparticles. *ChemPlusChem* **2016**, *81* (6), 526–534. https://doi.org/10.1002/cplu.201600007.

(9) Cheignon, C.; Heurté, M.; Knighton, R. C.; Kassir, A. A.; Lecointre, A.; Nonat, A.; Boos, A.; Christine, C.; Asfari, Z.; Charbonnière, L. J. Investigation of the Supramolecular Assembly of Luminescent Lanthanide Nanoparticles Surface Functionalized by P-Sulfonato-Calix[4]Arenes with Charged Aromatic Compounds. *Eur. J. Inorg. Chem.* **2021**, *2021* (36), 3761–3770. https://doi.org/10.1002/ejic.202100546.

(10) Kassir, A. A.; Cheignon, C.; Charbonnière, L. J. Exploitation of Luminescent Lanthanide Nanoparticles for a Sensitivity-Enhanced ELISA Detection Method. *Anal. Chem.* **2024**. https://doi.org/10.1021/acs.analchem.3c04821.

(11) Charpentier, C.; Cifliku, V.; Goetz, J.; Nonat, A.; Cheignon, C.; Cardoso Dos Santos, M.; Francés-Soriano, L.; Wong, K.-L.; Charbonnière, L. J.; Hildebrandt, N. Ultrabright Terbium Nanoparticles for FRET Biosensing and in Situ Imaging of Epidermal Growth Factor Receptors. *Chem. – Eur. J.* **2020**, *26* (64), 14602–14611. https://doi.org/10.1002/chem.202002007.

(12) Wang, F.; Zhang, Y.; Fan, X.; Wang, M. Facile Synthesis of Water-Soluble $LaF_3 : Ln^{3+}$ Nanocrystals. *J. Mater. Chem.* **2006**, *16* (11), 1031–1034. https://doi.org/10.1039/B518262J.

(13) Denton, A. R.; Ashcroft, N. W. Vegard's Law. *Phys. Rev. A* **1991**, *43* (6), 3161–3164. https://doi.org/10.1103/PhysRevA.43.3161.

(14) Shannon, R. D. Revised Effective Ionic Radii and Systematic Studies of Interatomic Distances in Halides and Chalcogenides. *Acta Crystallogr. A* **1976**, *32* (5), 751–767. https://doi.org/10.1107/S0567739476001551.

(15) Brixner, L. H.; Crawford, M. K.; Hyatt, G.; Carnall, W. T.; Blasse, G. Structure and Luminescence of the $La_{1-x}Gd_x F_3$ System. *J. Electrochem. Soc.* **1991**, *138* (1), 313. https://doi.org/10.1149/1.2085562.

(16) Liang, C.; Wang, Z.; Zhang, Y.; Duan, W.; Yue, W.; Ding, Y.; Wei, W. Effect of La/Gd Ratios on Phase, Morphology, and Fluorescence Properties of $La_xGd_{1-x}F_3$:Nd^{3+} Nanocrystals. *CrystEngComm* **2014**, *16* (23), 4963–4966. https://doi.org/10.1039/C3CE42629G.

(17) Wang, F.; Han, Y.; Lim, C. S.; Lu, Y.; Wang, J.; Xu, J.; Chen, H.; Zhang, C.; Hong, M.; Liu, X. Simultaneous Phase and Size Control of Upconversion Nanocrystals through Lanthanide Doping. *Nature* **2010**, *463* (7284), 1061–1065. https://doi.org/10.1038/nature08777.

(18) Nosov, V. G.; Betina, A. A.; Bulatova, T. S.; Guseva, P. B.; Kolesnikov, I. E.; Orlov, S. N.; Panov, M. S.; Ryazantsev, M. N.; Bogachev, N. A.; Skripkin, M. Y.; Mereshchenko, A. S. Effect of Gd^{3+}, La^{3+}, Lu^{3+} Co-Doping on the Morphology and Luminescent Properties of $NaYF_4$:Sm^{3+} Phosphors. *Materials* **2023**, *16* (6), 2157. https://doi.org/10.3390/ma16062157.

(19) Shao, F.; Ren, Z. Y.; Lu, C. J.; Yang, Y. D.; Zhan, Q.; Li, Z. P.; Chen, J. K.; Wu, Y.; Meng, K. K.; Xu, X. G.; Miao, J.; Jiang, Y. Self-Assembled Hexagonal $Lu_{1-x}In_xFeO_3$ Nanopillars Embedded in Orthorhombic $Lu_{1-x}In_xFeO_3$ Nanoparticle Matrixes as Room-Temperature Multiferroic Thin Films for Memory Devices and Spintronic Applications. *ACS Appl. Nano Mater.* **2020**, *3* (8), 7516–7523. https://doi.org/10.1021/acsanm.0c01139.

(20) Joseph, E.; Singhvi, G. Chapter 4 - Multifunctional Nanocrystals for Cancer Therapy: A Potential Nanocarrier. In *Nanomaterials for Drug Delivery and Therapy*; Grumezescu, A. M., Ed.; William Andrew Publishing, 2019; pp 91–116. https://doi.org/10.1016/B978-0-12-816505-8.00007-2.

(21) Labied, L.; Rocchi, P.; Doussineau, T.; Randon, J.; Tillement, O.; Lux, F.; Hagège, A. Taylor Dispersion Analysis Coupled to Inductively Coupled Plasma-Mass Spectrometry for Ultrasmall Nanoparticle Size Measurement: From Drug Product to Biological Media Studies. *Anal. Chem.* **2021**, *93* (3), 1254–1259. https://doi.org/10.1021/acs.analchem.0c03988.

(22) Ma, L.; Chen, W.-X.; Zheng, Y.-F.; Zhao, J.; Xu, Z. Microwave-Assisted Hydrothermal Synthesis and Characterizations of PrF_3 Hollow Nanoparticles. *Mater. Lett.* **2007**, *61* (13), 2765–2768. https://doi.org/10.1016/j.matlet.2006.04.124.

(23) Wang, X.; Li, Y. Fullerene-Like Rare-Earth Nanoparticles. *Angew. Chem. Int. Ed.* **2003**, *42* (30), 3497–3500. https://doi.org/10.1002/anie.200351006.

(24) Wang, X.; Li, Y. Rare-Earth-Compound Nanowires, Nanotubes, and Fullerene-Like Nanoparticles: Synthesis, Characterization, and Properties. *Chem. – Eur. J.* **2003**, *9* (22), 5627–5635. https://doi.org/10.1002/chem.200304785.

(25) Mittelheisser, V.; Coliat, P.; Moeglin, E.; Goepp, L.; Goetz, J. G.; Charbonniere, L. J.; Pivot, X.; Detappe, A. Optimal Physicochemical Properties of Antibody-Nanoparticle Conjugates for Improved Tumor Targeting. *Adv. Mater.* **2022**, *34* (24), 2110305. https://doi.org/10.1002/adma.202110305.

(26) Bünzli, J.-C. G. Lanthanide Luminescence for Biomedical Analyses and Imaging. *Chem. Rev.* **2010**, *110* (5), 2729–2755. https://doi.org/10.1021/cr900362e.

(27) Aebischer, A.; Gumy, F.; Bünzli, J.-C. G. Intrinsic Quantum Yields and Radiative Lifetimes of Lanthanide Tris(Dipicolinates). *Phys. Chem. Chem. Phys.* **2009**, *11* (9), 1346–1353. https://doi.org/10.1039/B816131C.

(28) Chauvin, A.; Gumy, F.; Imbert, D.; Bünzli, J. G. Europium and Terbium Tris(Dipicolinates) as Secondary Standards for Quantum Yield Determination. *Spectrosc. Lett.* **2004**, *37* (5), 517–532. https://doi.org/10.1081/SL-120039700.

(29) Adusumalli, V. N. K. B.; Mrówczyńska, L.; Kwiatek, D.; Piosik, Ł.; Lesicki, A.; Lis, S. Ligand-Sensitised LaF_3 :Eu^{3+} and SrF_2 :Eu^{3+} Nanoparticles and in Vitro Haemocompatiblity Studies. *ChemMedChem* **2021**, *16* (10), 1640–1650. https://doi.org/10.1002/cmdc.202100028.

(30) Liu, Y.; Zhang, J.; Zhang, C.; Jiang, J.; Jiang, H. High Efficiency Green Phosphor $Ba_9Lu_2Si_6O_{24}$:Tb^{3+}: Visible Quantum Cutting via Cross-Relaxation Energy Transfers. *J. Phys. Chem. C* **2016**, *120* (4), 2362–2370. https://doi.org/10.1021/acs.jpcc.5b11790.

(31) Álvarez-Ramos, M. E.; Félix-Domínguez, F.; Carrillo-Torres, R. C.; Saavedra-Rodríguez, G. Tb3+-Tb3+ Cross-Relaxation Study under Novel Experimental Technique: Simultaneous Laser Excitation at UV–Vis. *Spectrochim. Acta. A. Mol. Biomol. Spectrosc.* **2023**, *288*, 122136. https://doi.org/10.1016/j.saa.2022.122136.

(32) Valeur, B.; Berberan-Santos, M. N. Time-Resolved Fluorescence Techniques. In *Molecular Fluorescence: Principles and Applications*; Wiley-VCH, 2012; pp 285–325. https://doi.org/10.1002/9783527650002.

(33) Auzel, F. A Fundamental Self-Generated Quenching Center for Lanthanide-Doped High-Purity Solids. *J. Lumin.* **2002**, *100* (1), 125–130. https://doi.org/10.1016/S0022-2313(02)00457-X.

(34) Johnson, N. J. J.; He, S.; Diao, S.; Chan, E. M.; Dai, H.; Almutairi, A. Direct Evidence for Coupled Surface and Concentration Quenching Dynamics in Lanthanide-Doped Nanocrystals. *J. Am. Chem. Soc.* **2017**, *139* (8), 3275–3282. https://doi.org/10.1021/jacs.7b00223.

(35) Wei, W.; Chen, G.; Baev, A.; He, G. S.; Shao, W.; Damasco, J.; Prasad, P. N. Alleviating Luminescence Concentration Quenching in Upconversion Nanoparticles through Organic Dye Sensitization. *J. Am. Chem. Soc.* **2016**, *138* (46), 15130–15133. https://doi.org/10.1021/jacs.6b09474.

(36) Hildebrandt, N.; Charbonnière, L. J.; Löhmannsröben, H.-G. Time-Resolved Analysis of a Highly Sensitive Förster Resonance Energy Transfer Immunoassay Using Terbium Complexes as Donors and Quantum Dots as Acceptors. *J. Biomed. Biotechnol.* **2007**, *2007*, 79169. https://doi.org/10.1155/2007/79169.

(37) Zhou, S.; Zheng, W.; Chen, Z.; Tu, D.; Liu, Y.; Ma, E.; Li, R.; Zhu, H.; Huang, M.; Chen, X. Dissolution-Enhanced Luminescent Bioassay Based on Inorganic Lanthanide Nanoparticles. *Angew. Chem. Int. Ed.* **2014**, *53* (46), 12498–12502. https://doi.org/10.1002/anie.201405937.

(38) Kassir, A. A.; Cheignon, C.; Charbonnière, L. J. Exploitation of Luminescent Lanthanide Nanoparticles for a Sensitivity-Enhanced ELISA Detection Method. *Anal. Chem.* **2024**, *96* (5), 2107–2116. https://doi.org/10.1021/acs.analchem.3c04821.

(39) Peterson, K. L.; Margherio, M. J.; Doan, P.; Wilke, K. T.; Pierre, V. C. Basis for Sensitive and Selective Time-Delayed Luminescence Detection of Hydroxyl Radical by Lanthanide Complexes. *Inorg. Chem.* **2013**, *52* (16), 9390–9398. https://doi.org/10.1021/ic4009569.

Table of contents

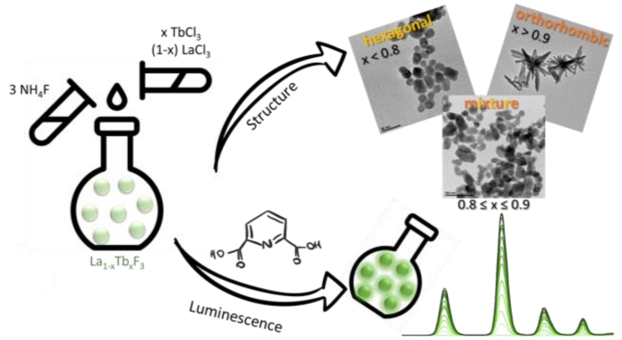

A systematic study of the size, structure and luminescence properties of a series of Tb doped LaF_3 nanoparticles has been realized to identify the best Tb doping rate for the design of a luminescent nanoprobe for bio-analytical applications. From this study, 40% Tb doped LaF_3 nanoparticles appear as the best candidate, being among the most colloidally stable, monodisperse rounded nanoparticles and exhibiting a long luminescence lifetime and high brightness when photosensitized by an appropriate antenna.